ORIGINAL RESEARCH ARTICLE

Modelling and simulation for defect detection in hydroelectric penstock using infrared thermography

Ho Jong Kim[1,2], Rakish Shrestha[3,†], Samman Singh Pradhan[3,†], Prithvi Gurung[3], Prabesh Bhattarai[3,†], Nirjal Lamichhane[3], Cheol Sang Kim[1,*], Ranjit Shrestha[3,*]

[1] *Division of Mechanical Design Engineering, Chonbuk National University, Jeonju 561756, Republic of Korea*

[2] *Changhae Eng Co., Ltd., 15, Wonmanseong-ro, Deokjin-gu, Jeonju-si, Jeollabuk-do 54854, Republic of Korea*

[3] *Department of Mechanical Engineering, School of Engineering, Kathmandu University, Dhulikhel 6250, Kavrepalanchok, Nepal*

* Corresponding authors: Cheol Sang Kim, chskim@jbnu.ac.kr; Ranjit Shrestha, ranjit.shrestha@ku.edu.np

† *These authors contributed equally.*

ABSTRACT

Modelling and simulation have now become standard methods that serve to cut the economic costs of R&D for novel advanced systems. This paper introduces the study of modelling and simulation of the infrared thermography process to detect defects in the hydroelectric penstock. A 3-D penstock model was built in ANSYS version 19.2.0. Flat bottom holes of different sizes and depths were created on the inner surface of the model as an optimal scenario to represent the subsurface defect in the penstock. The FEM was applied to mimic the heat transfer in the proposed model. The model's outer surface was excited at multiple excitation frequencies by a sinusoidal heat flux, and the thermal response of the model was presented in the form of thermal images to show the temperature contrast due to the presence of defects. The harmonic approximation method was applied to calculate the phase angle, and its relationship with respect to defect depth and defect size was also studied. The results confirmed that the FEM model has led to a better understanding of lock-in infrared thermography and can be used to detect subsurface defects in the hydroelectric penstock.

Keywords: penstock; subsurface defects; non-destructive testing and evaluation; infrared thermography; lock-in thermography; thermal image; phase angle

1. Introduction

Hydroelectricity is one of the oldest sources of renewable energy, with low operation and maintenance. The components of a hydropower plant are basically classified as civil engineering structures, hydro-mechanical components, and electro-mechanical equipment. A penstock is a mechanical component that is a conduit or tunnel connecting a reservoir or forebay to the hydroelectric turbine. Penstock has to withstand hydraulic pressure under static as well as dynamic conditions[1–3]. The operating conditions and maintenance of the penstock are critical factors for efficient power generation and the safety of plant workers. Penstock is vulnerable to both external and internal damages due to factors such as construction flaws, pressure differences, temperature differences, design, and service loads. The flow intensity within the penstock can vary, whether due to routine activities like valve adjustments or unexpected issues like hydraulic component failures. These fluctuations in flow velocity lead to abrupt pressure changes. Cavitation, a concerning effect, can occur when the

pressure reaches vapor-equivalent levels. This phenomenon has adverse consequences for hydraulic systems, including reduced flow capacity, disturbances in the flow, decreased efficiency of pumps and turbines, and the potential for damage to pipe materials. It's crucial to closely monitor these effects in their early stages to safeguard the structural integrity of the hydropower system[4–6]. Inspection of the inner surface of penstock becomes a major challenge as physical examinations could cause damage to the original condition. Non-destructive testing (NDT) techniques like X-ray, Ultrasound, Eddy Current, and Magnetic Resistance Inspection have been used to conduct inspections where physical examination is not possible. However, these techniques are slow and lengthy that require halting the energy production and dewatering of penstock, which can be factors in economic loss[7–9].

Infrared thermography (IRT) has been gaining vast attention in the diagnosis and monitoring of structural components in the last few decades. IRT is a non-destructive, non-intrusive, and non-contact technique that allows the mapping of thermal patterns and provides real-time and reliable data with increased sensitivity and spatial resolution. Hence, it is believed that IRT would be able to surpass the aforementioned inspection techniques as it can conduct inspection during the working of the penstock and a large surface area can be inspected over a short time[10]. The detailed theory of IRT can be reviewed in the literature[11–14].

In this work, modelling and simulation of the lock-in infrared thermography inspection process for detecting artificial subsurface defects in scale model penstocks are presented. At first, the finite element model of a test sample with flat-bottomed holes of varying size and depth was modelled in 'ANSYS 19.0' as a best-case scenario to represent real sub-surface defects, as the difference between real subsurface defects and flat-bottomed holes is relatively small. Then, the developed model was stimulated by a sinusoidal heat flux to simulate lock-in infrared thermography, which makes it possible to optimize the experimental parameters without the need for extensive, time-consuming, and potentially expensive preliminary experiments. Finally, a transient thermal and phase contrast analysis was performed to investigate the effects of defect size and depth, as well as modulation frequency, on defect detectability.

2. Lock-in thermography

Lock-in thermography (LIT) is a technique derived from photothermal radiometry. **Figure 1** illustrates the principle of defect detection by LIT. During the process of LIT, a modulated heat source in the form of a periodic wave is injected into the sample surface under investigation. The injected heatwave causes the temperature at each pixel on the sample surface to vary over time. The presence of subsurface defects can lead to a difference in the raw thermal images at each pixel. The location, sizes and depth of the defects can be explored by computing phase angle and or amplitude data from the raw thermal images. Phase angle data can eliminate the influences of uneven heating and surrounding reflections[15–18]. Hence, phase angle data is of interest in this research.
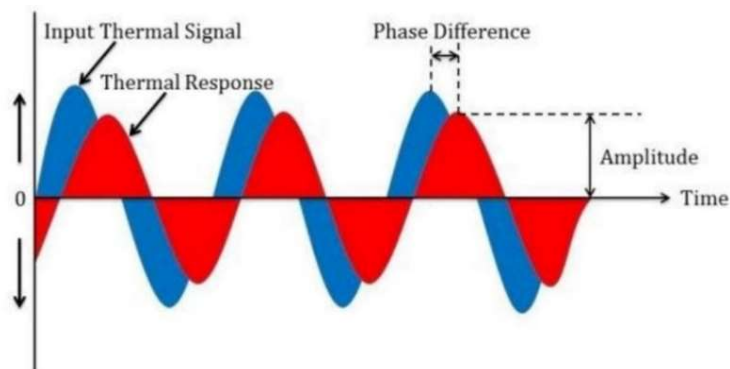

Figure 1. Principle of defect detection by LIT[13].

For a planar semi-infinite sample heated by a modulated heat source in the form of periodic wave, the temperature T (°C) can be expressed as Equation (1)[15–17],

$$T_{z,t} = T_0 e^{-\frac{z}{\mu}} \cos\left(\omega t - \frac{2\pi z}{\lambda}\right) = A(z)\cos[\omega t - \emptyset(z)] \tag{1}$$

where T_0 is the initial change in temperature [°C] caused by the heat source, z is the defect depth [m], $\mu = \sqrt{\frac{2\alpha}{\omega}} = \sqrt{\frac{\alpha}{\pi f}}$ is the thermal diffusion length [m] where $\alpha = \frac{k}{\rho.c_p}$ is the thermal diffusivity [m²/s] of the material being inspected, k is the thermal conductivity [W/mK], ρ is the density [kg/m³], c_p is the specific heat [J/kgK] at constant pressure, ω is the modulation frequency [rad/s], λ is thermal wavelength [m], A (z) is the thermal amplitude, $\emptyset(z)$ is the phase difference. Equation (1) tells that phase depends on defect depth and thermal diffusion length, whereas thermal diffusion length is related to properties such as thermal conductivity, density, and specific heat capacity of the material being inspected, as well as the modulation frequency.
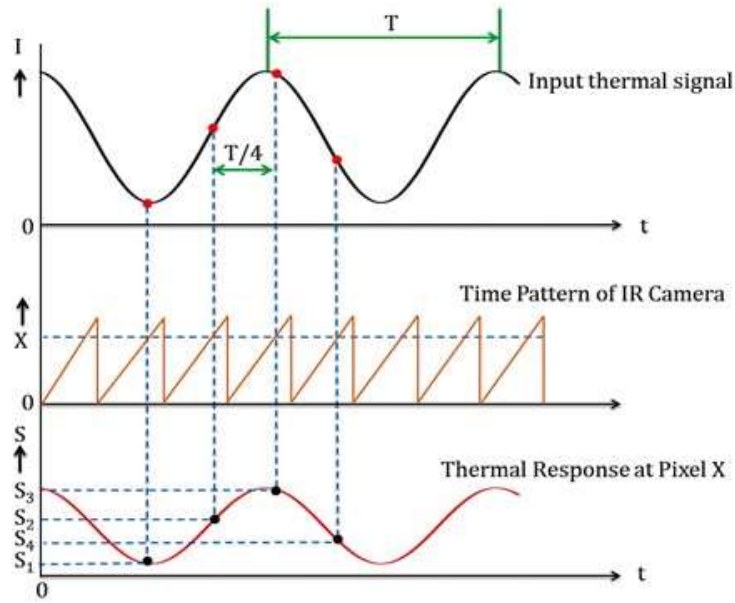
Figure 2. Principle of computation of phase angle by using Harmonic approximation[12].

If S_1, S_2, S_3, and S_4 are four equidistant thermal data in a complete period as shown in **Figure 2**, then phase can be expressed by Equation (2)[15–17],

$$\emptyset = \tan^{-1}\left(\frac{S_1 - S_3}{S_2 - S_4}\right) \tag{2}$$

The phase contrast, i.e., the difference between the phase angle of the defective area and the sound area, provides the defect information in terms of location, depth, and size. The phase contrast between the defective area and the sound area is expressed by Equation (3)[15,17],

$$\Delta\emptyset = \emptyset_d - \emptyset_S \tag{3}$$

where $\emptyset_d$ is the phase angle of the defective region and $\emptyset_S$ is the phase angle of the sound region.

3. Model configuration

The proposed 3-D penstock model is presented in **Figure 3**. The model geometry is defined by an outer diameter of 50 mm, a wall thickness of 12 mm, and a length of 100 mm. Flat bottom holes were created on the inner surface of the model as an optimal scenario to represent the subsurface defect in the real penstock. Two cases of defects, one with constant size and varying depth at the bottom part of the pipe as shown in **Figure 3**, and the other with constant depth and varying size at the top part of the pipe, which is not visible in **Figure 3**, were considered to study the effect of defect geometry on thermal response. **Figure 4a** shows the first case

3

where defects A, B, C, and D have a constant diameter of 12 mm and varying depths of 2, 3, 4, and 5 mm, respectively. **Figure 4b** shows the second case where defects E, F, G, and H have a constant depth of 5 mm and varying diameters of 6, 8, 10, and 12 mm, respectively. **Table 1** presents the geometrical parameters and the material properties of the model. A tetrahedral meshing was adapted considering physical preference as mechanical and element size 0.5 mm. The resultant mesh had 1,111,238 nodes and 656,176 elements.

In the proposed model, the influence of radiative and convective heat transfer has been neglected. The boundary condition for the heat flux can be expressed as Equation (4)[15],

$$-\mathrm{k}.\nabla T = Q_\mathrm{o} \tag{4}$$

where Q_o is the term which describes the heat flux on the irradiated surface.

The sample was considered to be in equilibrium with the environment at room temperature before the experiment started, and the initial condition is expressed as Equation (5),

$$\mathrm{T(x,y,z,t=0)} = \mathrm{T_{amb}} = 22°\mathrm{C} \tag{5}$$

It was assumed that the front surface of the sample was subjected to plane harmonic heat, and Equation (6)[15,18] was used to simulate the nature of sinusoidal heat flux with film coefficient 5 W/m²°C and emissivity 0.95.

$$Q = \frac{Q_\mathrm{o}}{2}(1 + \cos(2\pi ft)) \tag{6}$$

where Q is incident heat flux power density, Q_0 is the intensity of heating resource, f is modulation frequency, and t is the time.

During simulation, two halogen lamps, each of 1 kW intensity, were considered. The time-step in this study is systematically configured as $\frac{2}{100 \mathrm{x} f}$, where 'f' signifies the modulation frequency. This approach facilitates the accurate capture of temporal variations in signals across a wide range of modulation frequencies, ensuring that the analysis remains tailored to the unique characteristics of each signal. Research[19,20] showed that any frequency in the range of 0.1 to 0.9 Hz can be used for LIT. In this study, heat flux was applied to the outer surface of the pipe at three random modulation frequencies of 0.5 Hz, 0.2 Hz, and 0.1 Hz, considering the diffusion length of the thermal signal.
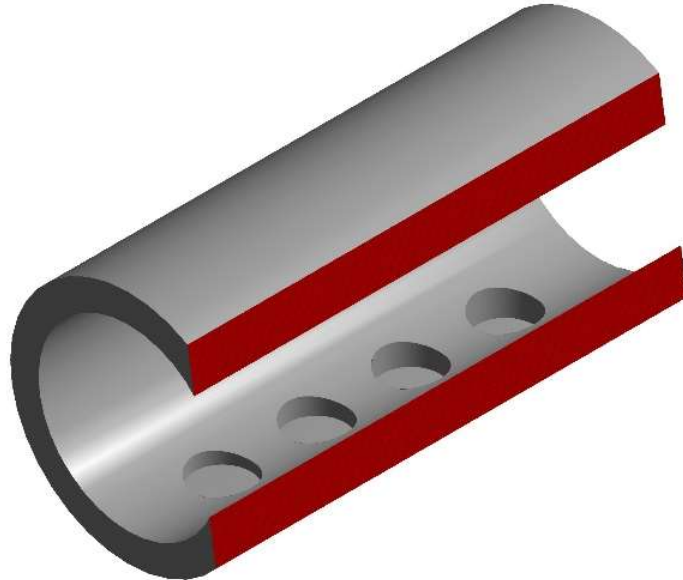
Figure 3. Geometry of the proposed 3-D penstock model.

(a)   **(b)**
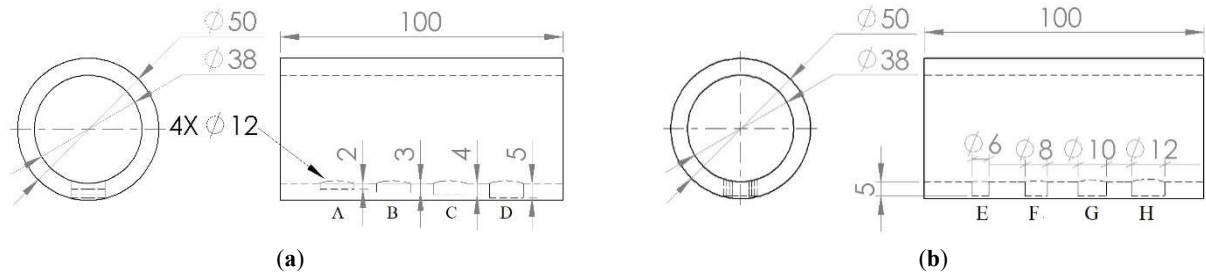
Figure 4. Schematic diagram of the proposed model. All dimensions are in mm.

Table 1. Geometrical parameters and thermal properties of the model.

Model	Parameters	Value	Units
Bounding box	Length X	50	mm
	Length Y	50	mm
	Length Z	100	mm
Properties	Volume	79,845	mm^3
	Mass	0.6188	kg
Material assigned: steel	Density	7750	kgm^{-3}
	Thermal conductivity	15.1	Wm^{-1}C^{-1}

4. Results and discussion

The previous research[21–24] confirmed that the depth of thermal waves is also dependent on the modulation frequency of the heat source, i.e., the lower the modulation frequency, the deeper the penetration of the thermal wave. Hence, a transient thermal analysis was conducted at three different modulation frequencies: 0.5 Hz, 0.2 Hz, and 0.1 Hz. The analysis was performed for two complete modulation cycles for each modulation frequency. **Figure 5** depicts a simulation view of the 3-D penstock model and the resulting temperature distribution at a modulation frequency of 0.1 Hz and a time of 15 s. **Figure 6a–c** depicts the raw thermal images at different time intervals for the modulation frequencies 0.5 Hz, 0.2 Hz, and 0.1 Hz, respectively, where defects A, B, C, and D are of constant diameter 12 mm and varying depths of 2, 3, 4, and 5 mm, respectively. Similarly, **Figure 7a–c** depicts the raw thermal images at different time intervals for the modulation frequencies 0.5 Hz, 0.2 Hz, and 0.1 Hz, respectively, where defects E, F, G & H are of varying diameters of 6, 8,10, and 12 mm and a constant depth of 5 mm. **Figure 8** depicts the periodical surface temperature evolution as a function of time for defects A, B, C, and D with respect to the sound area, and **Figure 9** depicts the periodical surface temperature evolution as a function of time for defects E, F, G, and H with respect to the sound area subjected to the modulation frequency of 0.1 Hz. **Figures 6–9** revealed that defective areas attained a high-temperature value than sound areas and are favorable for detection and estimating their position. It is also observed that thermal contrast is dependent on defect size, defect depth, and modulation frequency. As can be seen in **Figure 6**, defect D, being the shallowest defect, produced maximum thermal contrast at high modulation frequency whereas the other deeper defects C, B, and A are progressively detected at lower modulation frequencies. Similarly, in **Figure 7**, defect H, being the largest in size, produced maximum thermal contrast compared to smaller defects in all ranges of modulation frequency.
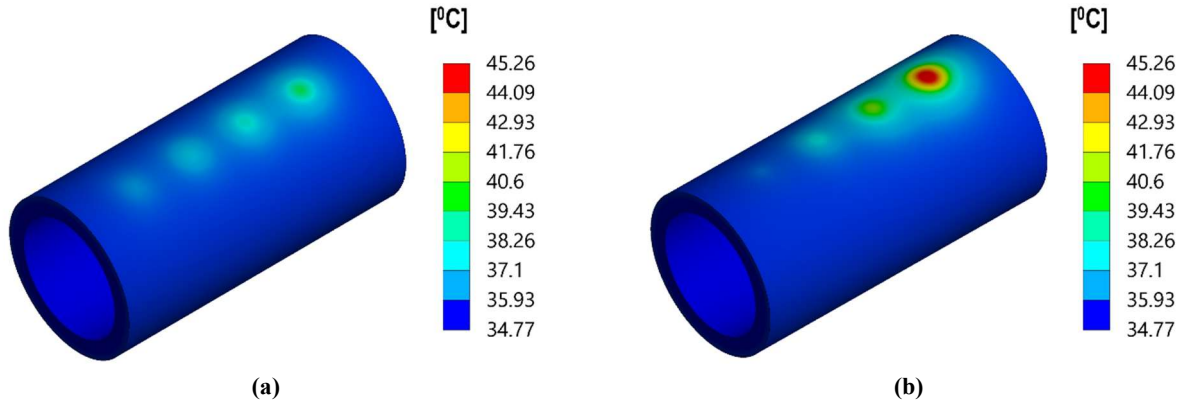
Figure 5. Simulation view of 3-D penstock model and the resulting temperature distribution via. simulated lock-in thermography at a modulation frequency of 0.1 Hz and time 15 sec in 'ANSYS 19.0', **(a)** Distribution of temperature for the defects with constant diameter and varying depths, and **(b)** Distribution of temperature for the defects with constant depth and varying diameter.

The temporal profile and time history as presented in **Table 2** were accounted for. The region of interest of 3 × 3 nodes at the center of each defect and in the adjacent sound area for each defect was selected. The average temperature data of selected nodes was considered, and Equation (2) was used to calculate the phase angle data.

Table 2. Details of simulated data considered during phase extraction.

Modulation frequency (Hz)	Period (s)	Modulation cycle (no.)	Image interval time (s)	Image considered wrt time (s)			
				1st	2nd	3rd	4th
0.5	2	2	0.50	2.00	2.50	3.00	3.50
0.2	5		1.25	5.00	6.25	7.50	8.75
0.1	10		2.50	10.0	12.50	15.00	17.50

To determine the optimum modulation frequency, an analysis was conducted on the phase contrast between the defects and the nearby sound regions. The phase contrast was acquired by subtracting the phase angle of the sound area, from the defective area as explained in Equation (3). **Figure 10** depicts the phase contrast for defects with constant size as a function of depths for different modulation frequencies. It is observed that the higher modulation frequency, 0.5 Hz, is limited to detecting only the shallowest defect with maximum phase contrast and is found ineffective for other deeper defects, whereas the medium and lower ranges of modulation frequencies, i.e., 0.2 Hz and 0.1 Hz, respectively, are found to be more effective in detecting deeper defects. Similarly, **Figure 11** depicts the phase contrast of defects with constant depth as a function of size at different modulation frequencies. It is observed that the higher modulation frequency is limited to detecting larger diameters only and is found ineffective for smaller ones, whereas the medium and lower modulation frequencies were found more appropriate to detect smaller diameters. Also, in between the medium and lower modulation frequencies, phase inversion occurred, and phase contrast may be positive and/or negative. Ultimately, a modulation frequency of 0.1 Hz can be recommended for the detection of defects in the sample penstock pipe under consideration, as it can provide reasonable thermal and phase contrast for the defects with respect to sizes and depths.
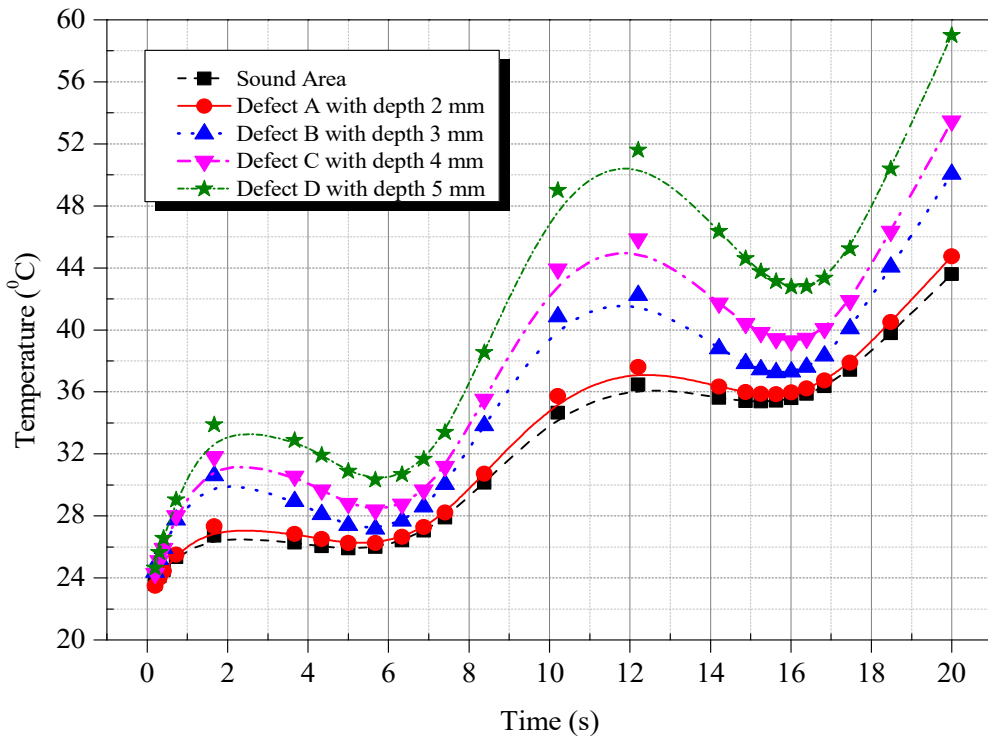
6
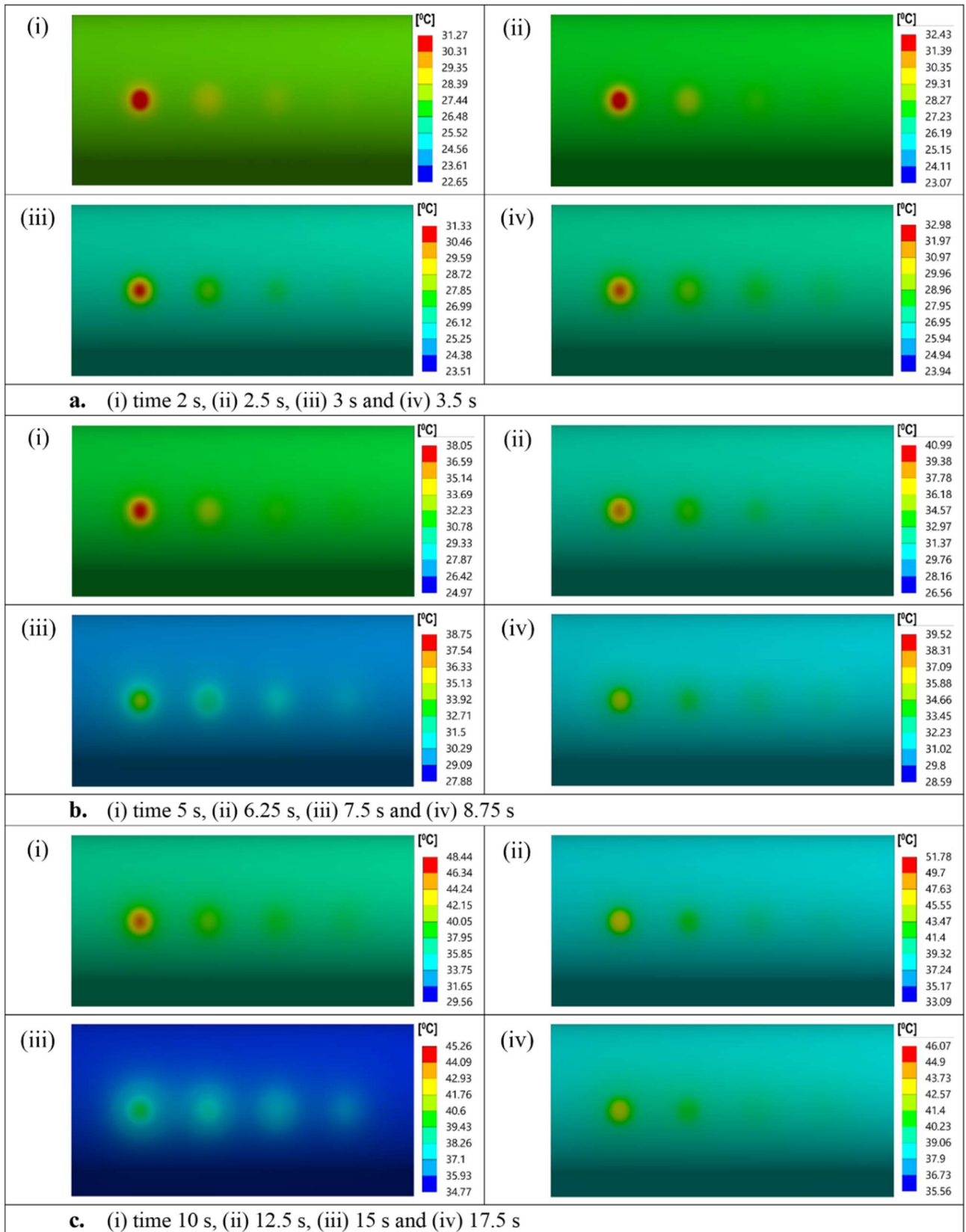
Figure 6. Raw thermal images obtained by simulated lock-in thermography as a function defect depth at different modulation frequencies; **(a)** 0.5 Hz, **(b)** 0.2 Hz, and **(c)** 0.1 Hz.
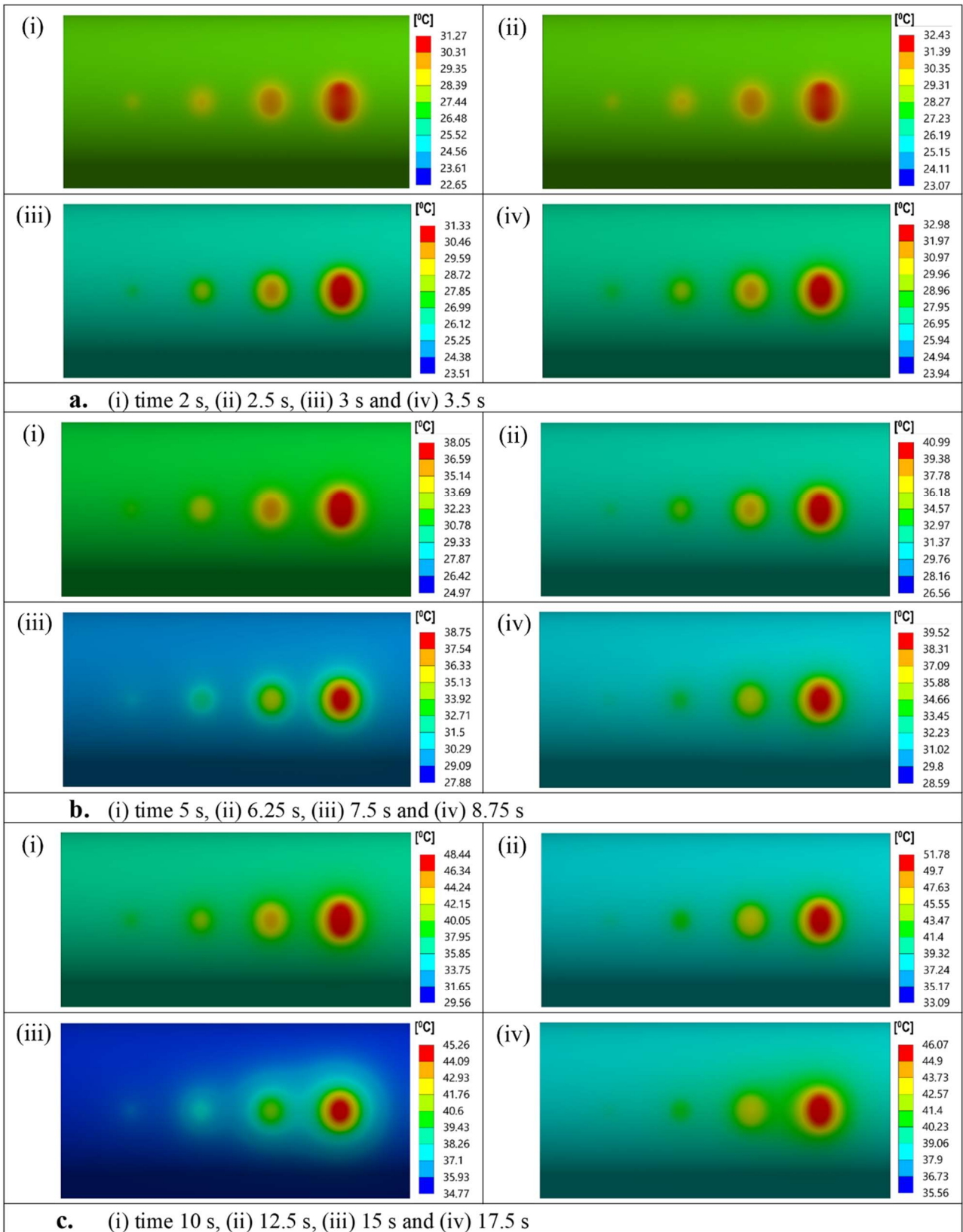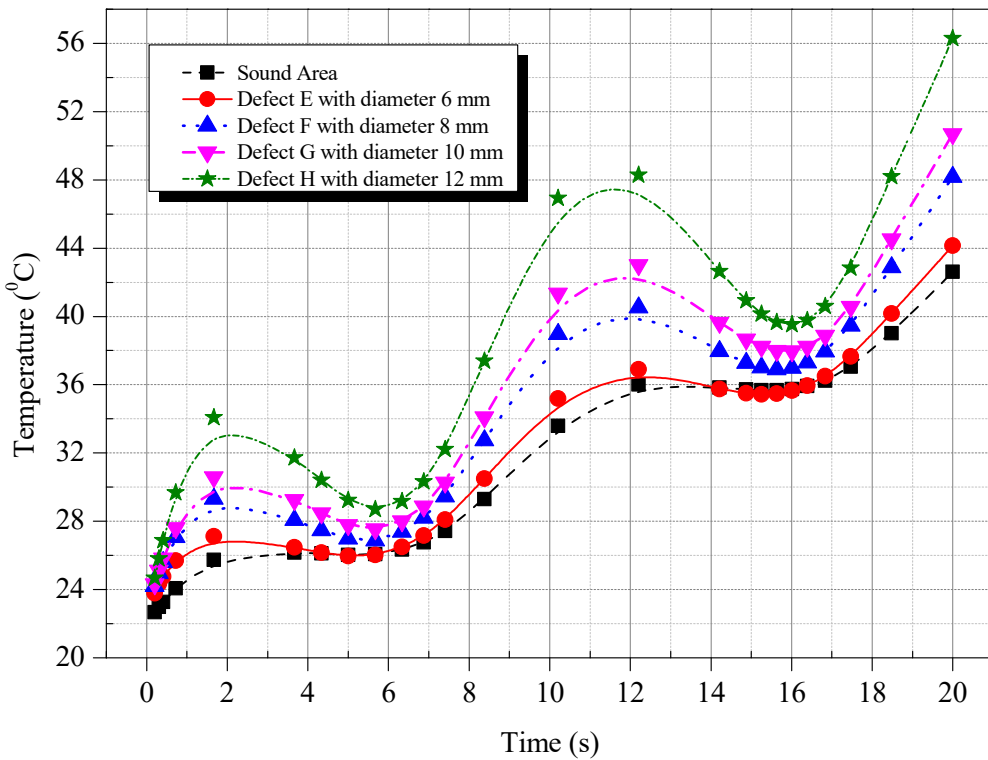
Figure 7. Raw thermal images obtained by simulated lock-in thermography as a function defect size at different modulation frequencies; **(a)** 0.5 Hz, **(b)** 0.2 Hz, and **(c)** 0.1 Hz.

Figure 8. Simulated periodical surface temperature evolution of sound and defective areas of uniform size and varying depth subjected to lock-in heating at a modulation frequency of 0.1 Hz.

Figure 9. Simulated periodical surface temperature evolution of sound and defective areas of uniform depth and varying diameter subjected to lock-in heating at a modulation frequency of 0.1 Hz.

9
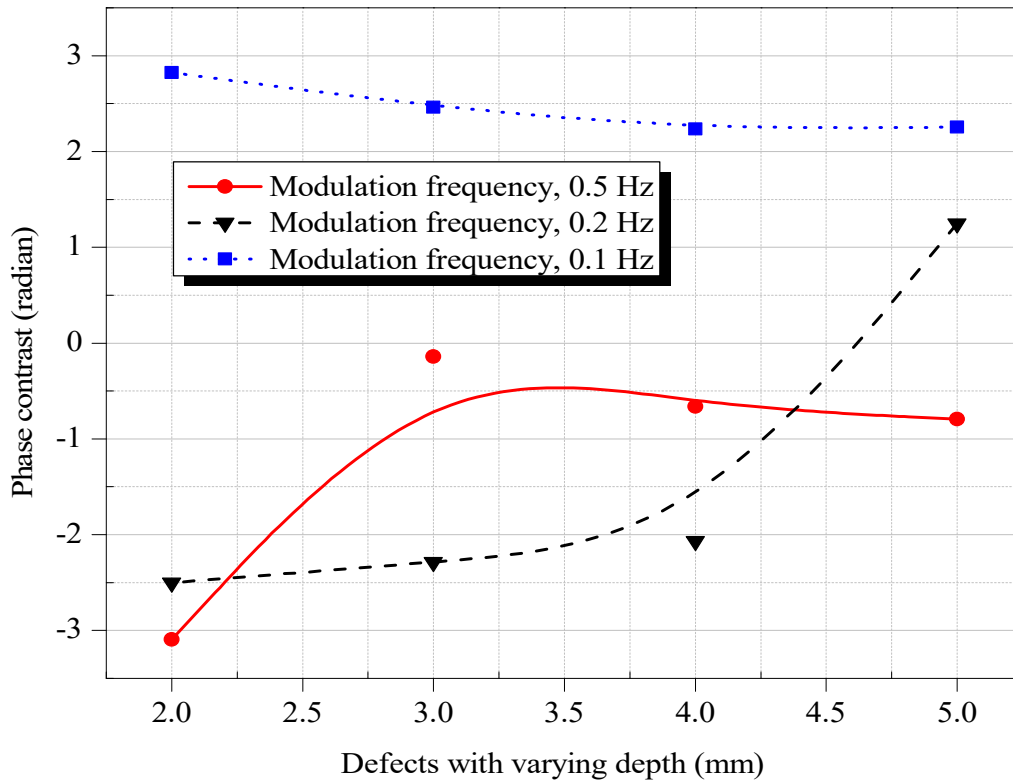
Figure 10. Phase contrast processed with harmonic approximation from the simulated lock-in thermography as a function defect depth at different modulation frequencies.
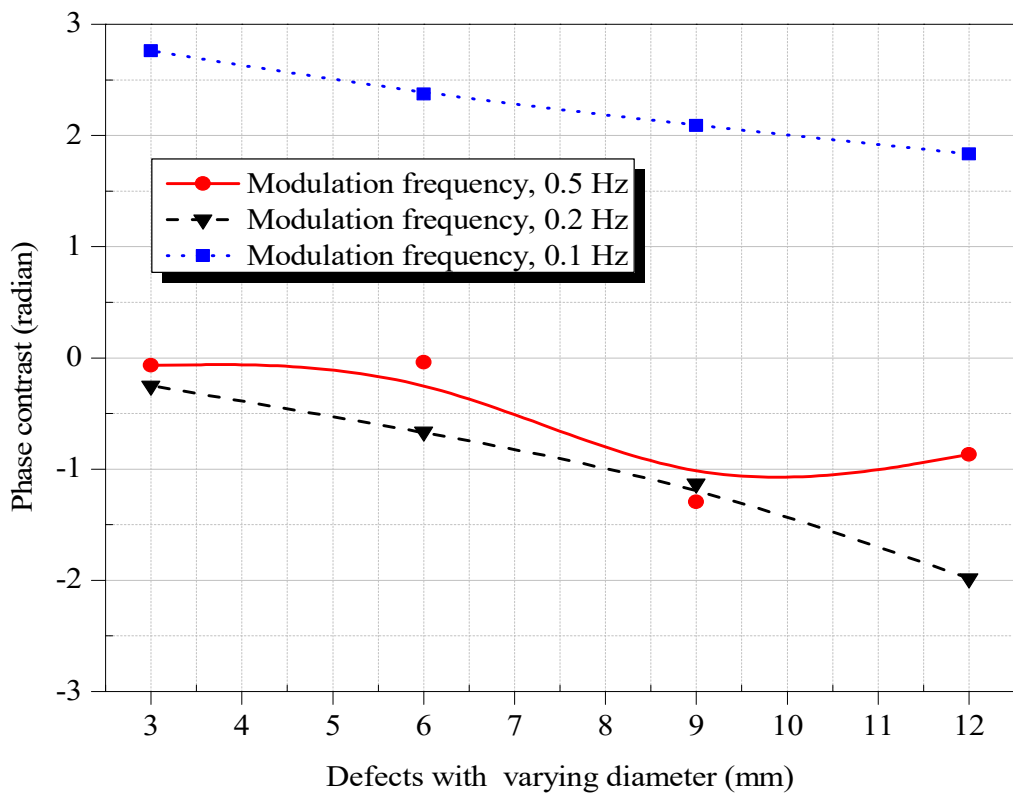
Figure 11. Phase contrast processed with harmonic approximation from the simulated lock-in thermography as a function defect size at different modulation frequencies.

5. Conclusions

This study investigated the use of lock-in infrared thermography to detect defects in the hydroelectric penstock. The presented results demonstrated that modelling and simulation of the lock-in infrared thermography inspection process are possible and useful to understand and optimize the experimental results. The simulated thermal and phase data make it possible to optimize the modulation frequency adapted to the test sample. In future work, more modelling and simulations are planned to detect irregularities of different shapes, sizes, and depths in the penstock and to validate the obtained results experimentally.

Author contributions

Conceptualization, RS (Ranjit Shrestha); data curation, RS (Rakish Shrestha), SS, PG and PB; formal analysis, RS (Rakish Shrestha), SSP, PG, PB and HJK; funding acquisition, HJK; investigation, RS (Rakish Shrestha), SS, PG, PB and HJK; methodology, RS (Rakish Shrestha), SSP, PG and PB; project administration, RS (Ranjit Shrestha); resources, HJK; software, HJK; supervision, CSK and RS (Ranjit Shrestha); visualization, RS (Rakish Shrestha), SS, PG and PB; validation, RS (Ranjit Shrestha) and CSK; writing—original draft, RS (Rakish Shrestha), SS, PG, PB and HJK; writing—review and editing, RS (Ranjit Shrestha) and NL. All authors have read and agreed to the published version of the manuscript.

Acknowledgments

Conflict of interest

The authors declare no conflict of interest.

Abbreviations

IRT, infrared thermography; LIT, lock-in thermography; NDT, non-destructive testing.

References

1. Pradhan GL, Lacoul S, Bhat SS, Carpentier JM. Vision 2020: Hydropower—A vision for growth. *Hydro Nepal Journal of Water Energy and Environment* 2009; 4: 56–58. doi: 10.3126/hn.v4i0.1830
2. Singhal MK, Arun K. Optimum design of penstock for hydro projects. *International Journal of Energy and Power Engineering* 2015; 4(4): 216–226. doi: 10.11648/j.ijepe.20150404.14
3. Alam F, Alam Q, Reza S, et al. A review of hydropower projects in Nepal. *Energy Procedia* 2017; 110: 581–585. doi: 10.1016/j.egypro.2017.03.188
4. Government of Nepal, Ministry of Water Resources, Department of Electricity Development. *Design Guidelines for Water Conveyance System of Hydropower Projects*. Department of Electricity Development; 2006.
5. Aifaoui N, Affi Z, Abbes MS, et al. Design and modeling of mechanical systems—IV. In: Proceedings of the 8th Conference on Design and Modeling of Mechanical Systems, CMSM'2019; 18–20 March 2019; Hammamet, Tunisia.
6. Bergant A, Simpson AR, Tijsseling AS. Water hammer with column separation: A historical review. *Journal of Fluids and Structures* 2006; 22(2): 135–171. doi: 10.1016/j.jfluidstructs.2005.08.008
7. McStraw B. Inspection of steel penstocks and pressure conduits. In: *Facilities Instructions, Standards, and Techniques*. U.S. Department of the Interior; 2000.
8. Ma Z, Lu Y, Hu F, et al. The material comparison design of penstock pipe for a hydroelectric pumped storage station. *Journal of Physics: Conference Series* 2021; 2009(1): 012027. doi: 10.1088/1742-6596/2009/1/012027
9. Qu Z, Jiang P, Zhang W. Development and application of infrared thermography non-destructive testing techniques. *Sensors* 2020; 20(14): 3851. doi: 10.3390/s20143851
10. Yoo KH, Kim JH, Na MG, et al. On-power detection of wall-thinned defects using lock-in infrared thermography. *Nuclear Engineering and Design* 2014; 280: 542–549. doi: 10.1016/j.nucengdes.2014.10.008

11. Maldague XP. *Theory and Practice of Infrared Technology for Nondestructive Testing*. Wiley-Interscience; 2001.
12. Meola C, Carlomagno GM. Recent advances in the use of infrared thermography. *Measurement Science and Technology* 2004; 15(9): R27–R58. doi: 10.1088/0957-0233/15/9/r01
13. Czichos H. *Handbook of Technical Diagnostics*. Springer Berlin Heidelberg; 2013.
14. Vavilov V, Burleigh D. *Infrared Thermography and Thermal Nondestructive Testing*. Springer Cham; 2020.
15. Ranjit S, Kang K, Kim W. Investigation of lock-in infrared thermography for evaluation of subsurface defects size and depth. *International Journal of Precision Engineering and Manufacturing* 2015; 16(11): 2255–2264. doi: 10.1007/s12541-015-0290-z
16. Ranjit S, Choi M, Kim W. Quantification of defects depth in glass fiber reinforced plastic plate by infrared lock-in thermography. *Journal of Mechanical Science and Technology* 2016; 30(3): 1111–1118. doi: 10.1007/s12206-016-0215-5
17. Shrestha R, Park J, Kim W. Application of thermal wave imaging and phase shifting method for defect detection in Stainless steel. *Infrared Physics & Technology* 2016; 76: 676–683. doi: 10.1016/j.infrared.2016.04.033
18. Shrestha R, Kim W. Evaluation of coating thickness by thermal wave imaging: A comparative study of pulsed and lock-in infrared thermography—Part I: Simulation. *Infrared Physics & Technology* 2017; 83: 124–131. doi: 10.1016/j.infrared.2017.04.016
19. Chatterjee K, Tuli S, Pickering SG, Almond DP. A comparison of the pulsed, lock-in and frequency modulated thermography nondestructive evaluation techniques. *NDT & E International* 2011; 44(7): 655–667. doi: 10.1016/j.ndteint.2011.06.008
20. Wallbrink C, Wade SA, Jones R. The effect of size on the quantitative estimation of defect depth in steel structures using lock-in thermography. *Journal of Applied Physics* 2007; 101(10): 104907. doi: 10.1063/1.2732443
21. Shrestha R, Kim W. Non-destructive testing and evaluation of materials using active thermography and enhancement of signal to noise ratio through data fusion. *Infrared Physics & Technology* 2018; 94: 78–84. doi: 10.1016/j.infrared.2018.08.027
22. Shrestha R, Kim W. Evaluation of coating thickness by thermal wave imaging: A comparative study of pulsed and lock-in infrared thermography—Part II: Experimental investigation. *Infrared Physics & Technology* 2018; 92: 24–29. doi: 10.1016/j.infrared.2018.05.001
23. Shrestha R, Chung Y, Kim W. Wavelet transform applied to lock-in thermographic data for detection of inclusions in composite structures: Simulation and experimental studies. *Infrared Physics & Technology* 2019; 96: 98–112. doi: 10.1016/j.infrared.2018.11.008
24. Shrestha R, Choi M, Kim W. Thermographic inspection of water ingress in composite honeycomb sandwich structure: A quantitative comparison among lock-in thermography algorithms. *Quantitative InfraRed Thermography Journal* 2019; 18(2): 92–107. doi: 10.1080/17686733.2019.1697848